Investigation of shock waves in the relativistic Riemann problem: A comparison of viscous fluid dynamics to kinetic theory

I. Bouras,[1] E. Molnár,[2,3] H. Niemi,[2] Z. Xu,[1,2] A. El,[1] O. Fochler,[1] C. Greiner,[1] and D. H. Rischke[1,2]

[1]*Institut für Theoretische Physik, Johann Wolfgang Goethe-Universität, Max-von-Laue-Strasse 1, D-60438 Frankfurt am Main, Germany*

[2]*Frankfurt Institute for Advanced Studies, Ruth-Moufang-Strasse 1, D-60438 Frankfurt am Main, Germany*

[3]*KFKI, Research Institute of Particle and Nuclear Physics, H-1525 Budapest, P.O. Box 49, Hungary*

(Received 7 June 2010; published 27 August 2010)

We solve the relativistic Riemann problem in viscous matter using the relativistic Boltzmann equation and the relativistic causal dissipative fluid-dynamical approach of Israel and Stewart. Comparisons between these two approaches clarify and point out the regime of validity of second-order fluid dynamics in relativistic shock phenomena. The transition from ideal to viscous shocks is demonstrated by varying the shear viscosity to entropy density ratio η/s. We also find that a good agreement between these two approaches requires a Knudsen number $\mathrm{Kn} < 1/2$.

DOI: 10.1103/PhysRevC.82.024910 PACS number(s): 25.75.−q, 52.35.Tc, 24.10.Lx, 24.10.Nz

I. INTRODUCTION

One of the strongest arguments for studying a fully relativistic formulation of fluid dynamics is the large value of the elliptic flow coefficient v_2 measured in ultrarelativistic heavy-ion collisions at the Relativistic Heavy Ion Collider (RHIC) at Brookhaven National Laboratory (BNL) [1]. These measurements indicate that a new phase of matter, the quark-gluon plasma, is created, which behaves like an almost perfect fluid. An indication for this is the good agreement between experimental data and theoretical calculations using ideal fluid dynamics, where the viscous transport coefficients vanish; see, e.g. Refs., [2–4].

In nature, the viscous transport coefficients cannot vanish but must have lower bounds [5–7]. Small viscous corrections are always needed in fluid dynamics to make the flow laminar and stable. It was later confirmed by calculations within viscous fluid dynamics [8] and microscopic transport theory [9] that the shear viscosity has to be sufficiently small in order to keep the agreement with the v_2 data. These calculations suggest that the shear viscosity to entropy density ratio $\eta/s < 0.4$.

In heavy-ion collisions at ultrarelativistic energies the system expands very fast and gradients in the matter are very large. It is still an open question to what extent fluid dynamics is applicable in describing the dynamics of such a system. Fluid dynamics is an effective theory that describes the macroscopic evolution of the system close to thermal equilibrium. Its applicability requires that either the viscosity or the gradients are small, or both. On the other hand, microscopic transport models can be used for systems which are also strongly out of thermal equilibrium. Therefore, a comparison between the microscopic approach and fluid dynamics can provide the limits and accuracy of the fluid-dynamical description.

In this work we will compare solutions of the relativistic Boltzmann equation with those of second-order fluid dynamics as derived by Israel and Stewart (IS) [10–12]. Such a comparison has been previously presented for the Bjorken scaling solution [13] in Ref. [14]. The scaling solution provides a simple test case with (initially) arbitrarily large expansion rate. It was concluded that for a good agreement between the fluid-dynamical and kinetic calculations a Knudsen number $\mathrm{Kn} < 1/2$ is required. The Knudsen number is the ratio of the mean-free path of the particles and the length scale of the variation of macroscopic fields (such as the energy density). For the same scaling solution, an extension of the IS theory was studied and compared to the kinetic solutions in Ref. [15].

The Bjorken scaling solution is, however, restrictive in the sense that there are no pressure gradients in the local rest frame (LRF) of matter. In this paper we will complement these earlier works by studying the relativistic Riemann problem. This was already investigated in Refs. [16,17], and we continue this line of study with more extensive and detailed comparisons between the fluid-dynamical and transport approaches. The existing analytic solution in the perfect-fluid limit, i.e., for $\eta = 0$, makes it possible to check the numerical convergence of the approaches. To our best knowledge this type of study was never accomplished for relativistic shock phenomena.

The present work is yet another step toward understanding how highly energetic jets created in the initial stage of an ultrarelativistic heavy-ion collision interact with the hot and dense medium. If the latter is a strongly interacting fluid, one expects the creation of shock waves which resemble Mach cones. However, if matter is only weakly interacting, these shock waves should be smeared out and a clean Mach-cone signal cannot be observed [18].

The paper is organized as follows: In Sec. II the dissipative fluid-dynamical theory of Israel and Stewart is introduced. This is followed in Sec. III by a short introduction to the numerical methods we use. In Sec. IV the relativistic Riemann problem and its analytic solution in the perfect-fluid limit are presented. We demonstrate that numerical calculations using both approaches reproduce the analytic solutions very accurately. In Sec. V we show comparisons with nonzero viscosities and demonstrate how the agreement between the two approaches deteriorates with increasing viscosity. These results are then analyzed in terms of a relevant Knudsen number in order to estimate the applicability of the IS theory. As in the ideal case, we have found a scaling behavior of the relativistic Riemann problem with nonzero viscosity. This

is discussed in Sec. VI. Finally, conclusions are given in Sec. VII.

Our units are $\hbar = c = k = 1$; the metric is $g^{\mu\nu} = \mathrm{diag}(1, -1, -1, -1)$.

II. FROM KINETIC THEORY TO FLUID DYNAMICS

A. Definitions

In relativistic kinetic theory of simple gases matter is characterized by the invariant single-particle distribution function $f(x, p)$. The space-time evolution of $f(x, p)$ caused by particle motion and collisions is given by the relativistic Boltzmann transport equation [19,20],

$$p^\mu \partial_\mu f(x, p) = C[f(x, p)], \tag{1}$$

where $C[f(x, p)]$ is the collision integral and $p^\mu = (E, \mathbf{p})$ is the particle four-momentum. We assume that there are no external forces.

Macroscopic quantities can be obtained from the moments of the distribution function. The first moment is the particle four-flow,

$$N^\mu \equiv \int d\tilde{p} p^\mu f(x, p), \tag{2}$$

where $d\tilde{p} \equiv g d^3p/[(2\pi)^3 E]$ and g is the degeneracy factor counting internal degrees of freedom. The second moment defines the energy-momentum tensor,

$$T^{\mu\nu} \equiv \int d\tilde{p} p^\mu p^\nu f(x, p). \tag{3}$$

Similarly one can define higher moments of the distribution function, such as the third moment,

$$F^{\mu\nu\lambda} \equiv \int d\tilde{p} p^\mu p^\nu p^\lambda f(x, p). \tag{4}$$

The entropy four-current is defined as

$$S^\mu \equiv \int d\tilde{p} p^\mu f(x, p)\left[1 - \ln f(x, p)\right]. \tag{5}$$

The assumption of the conservation of particle number or charge and energy-momentum conservation in individual collisions leads to

$$\partial_\mu N^\mu \equiv \int d\tilde{p} p^\mu \partial_\mu f = \int d\tilde{p} C = 0, \tag{6}$$

$$\partial_\nu T^{\mu\nu} \equiv \int d\tilde{p} p^\mu p^\nu \partial_\nu f = \int d\tilde{p} p^\mu C = 0. \tag{7}$$

These are the conservation equations of relativistic fluid dynamics [21]. A similar equation resulting from the Boltzmann equation for the third moment gives the balance of fluxes,

$$\partial_\lambda F^{\mu\nu\lambda} \equiv \int d\tilde{p} p^\mu p^\nu p^\lambda \partial_\lambda f = \int d\tilde{p} p^\mu p^\nu C. \tag{8}$$

This will be discussed in the next section. The Boltzmann H theorem implies that the entropy production is positive and vanishes in equilibrium,

$$\partial_\mu S^\mu \geqslant 0. \tag{9}$$

The particle four-flow and energy-momentum tensor can be decomposed with respect to an arbitrary timelike four-vector u^μ, normalized as $u^\mu u_\mu = 1$. This is chosen in such a way that it can be interpreted as the collective four-velocity of the matter. The frame where $u^\mu = (1, 0, 0, 0)$ is called the local rest frame. With the help of the transverse projection operator $\Delta^{\mu\nu} = g^{\mu\nu} - u^\mu u^\nu$, the most general decomposition can be written as

$$N^\mu = n u^\mu + V^\mu, \tag{10}$$

$$T^{\mu\nu} = e u^\mu u^\nu - P\Delta^{\mu\nu} + W^\mu u^\nu + W^\nu u^\mu + \pi^{\mu\nu}, \tag{11}$$

where $n \equiv N^\mu u_\mu$ is the LRF particle density and $e \equiv u_\mu T^{\mu\nu} u_\nu$ is the LRF energy density. The spatial trace of the energy-momentum tensor, $P = -\frac{1}{3}\Delta_{\mu\nu} T^{\mu\nu}$, denotes the isotropic pressure. This is the sum of equilibrium pressure and bulk viscous pressure, $P = p(e, n) + \Pi$. The flow of particles in the LRF is

$$V^\mu = \Delta^\mu_\nu N^\nu, \tag{12}$$

while the flow of energy-momentum in the LRF is

$$W^\mu = \Delta^{\mu\alpha} T_{\alpha\beta} u^\beta. \tag{13}$$

The heat flow q^μ is defined as

$$q^\mu = W^\mu - h V^\mu, \tag{14}$$

where $h = (e + p)/n$ is the enthalpy per particle.

The shear-stress tensor, $\pi^{\mu\nu} = T^{\langle\mu\nu\rangle}$, where

$$T^{\langle\mu\nu\rangle} \equiv \left(\tfrac{1}{2}\left(\Delta^\mu_\alpha \Delta^\nu_\beta + \Delta^\nu_\alpha \Delta^\mu_\beta\right) - \tfrac{1}{3}\Delta^{\mu\nu}\Delta_{\alpha\beta}\right) T^{\alpha\beta}, \tag{15}$$

is that part of $T^{\mu\nu}$ that is symmetric, traceless, and orthogonal to the flow velocity.

In equilibrium all dissipative terms vanish, that is, $\Pi = V^\mu = W^\mu = \pi^{\mu\nu} = 0$, therefore the particle four-current and energy-momentum tensor take a simpler form,

$$N^\mu_0 = n_0 u^\mu, \tag{16}$$

$$T^{\mu\nu}_0 = e_0 u^\mu u^\nu - p_0 \Delta^{\mu\nu}, \tag{17}$$

where the subscript "0" indicates local thermodynamical equilibrium. In local equilibrium, the particle four-current N^μ_0, the energy-momentum tensor $T^{\mu\nu}_0$, and the entropy four-current S^μ_0, are uniquely defined for any timelike four-velocity u^μ. The LRF frame particle density and energy density are given by $n_0 \equiv N^\mu_0 u_\mu$ and $e_0 \equiv u_\mu T^{\mu\nu}_0 u_\nu$, respectively.

For a system that deviates from local thermodynamical equilibrium, the definition of the flow velocity may follow Eckart [22] or Landau and Lifshitz [23]. Using Eckart's definition of the flow velocity,

$$u^\mu_E = \frac{N^\mu}{\sqrt{N^\nu N_\nu}}, \tag{18}$$

the LRF flow of particles vanishes, $V^\mu = 0$, while the flow of energy is given by the heat flow, $W^\mu = q^\mu$.

In Landau's frame the flow of matter is tied to the flow of energy,

$$u^\mu_L = \frac{T^{\mu\nu} u_\nu}{\sqrt{u_\alpha T^{\beta\alpha} T_{\beta\gamma} u^\gamma}}; \tag{19}$$

hence the flow of energy-momentum vanishes, $W^\mu = 0$.

For processes close to equilibrium, the above definitions and decompositions are related to each other [24]. Therefore up to second order in deviations from local equilibrium, that is, $\delta u^\mu \sim q^\mu/e \ll 1$, we get

$$u_L^\mu = u_E^\mu + \frac{q^\mu}{e+p}. \tag{20}$$

This means that the nonequilibrium part of the particle four-flow in Landau's frame is related to the heat flow in Eckart's frame, that is, $V^\mu = -q^\mu/h$.

B. Fluid dynamics as an approximation to kinetic theory

Fluid dynamics is an effective theory for the slow, long-wavelength dynamics of a given system. For systems with well-defined quasiparticles, fluid dynamics can be derived in terms of a power series in the Knudsen number

$$\mathrm{Kn} = \frac{\lambda_{\mathrm{mfp}}}{L}, \tag{21}$$

where λ_{mfp} is the mean-free path of the particles and L is a macroscopic length scale over which macroscopic fields such as energy density, particle density, or temperature vary. Fluid dynamics as an effective theory can be systematically improved by successively including higher-order terms in Kn [15].

To zeroth order in Kn we obtain an effective theory that does not contain any powers of Kn, corresponding to the limit $\mathrm{Kn} \to 0$, that is, the (unphysical) limit where $\lambda_{\mathrm{mfp}} \to 0$. This corresponds to infinite scattering rates, and thus the system instantaneously assumes local thermodynamical equilibrium. This is the perfect-fluid limit. To first order in Kn, we obtain the relativistic generalization of Navier-Stokes theory. This effective theory is plagued by instabilities and acausalities [25–27]. These problems can be circumvented by including terms of second order in Kn, such as in the fluid-dynamical theory of Israel and Stewart used in this work. The fluid-dynamical limit can be derived for any kind of system, that is, its applicability is not restricted to dilute gases, as is the case for the Boltzmann equation. However, since it is an expansion around the perfect-fluid limit, we expect its validity to be restricted to dynamics close to local thermodynamical equilibrium.

The coefficients of fluid dynamics as an effective theory can be computed by matching to an underlying microscopic theory. In our case, this is the kinetic theory of ultrarelativistic Boltzmann particles, described by the Boltzmann equation with elastic binary collisions. Note, however, that the matching procedure is not unique [28].

In our case the matching procedure is as follows. We expand the single-particle distribution function around local thermodynamical equilibrium, $f(x,p) = f_0(x,p) + \delta f$, where δf measures the deviation from the equilibrium distribution function

$$f_0(x,p) \equiv (e^{\beta p^\mu u_\mu}/\lambda + a)^{-1}. \tag{22}$$

Here $a = -1$ $(+1)$ corresponds to bosons (fermions), and $a = 0$ corresponds to Boltzmann particles. The inverse temperature is given by $\beta(x) = 1/T(x)$ and $\lambda(x) = e^{\beta(x)\mu(x)}$ is the fugacity. The validity of the expansion around f_0 requires that $\phi = \delta f/f_0 \ll 1$. In order to match to fluid dynamics as an expansion in powers of Kn, one possibility is to assume that ϕ is a series in powers of Kn. This approach was pioneered by Hilbert, and by Chapman and Enskog [20].

Another method was proposed by Grad [29] and was generalized to relativistic systems by Israel and Stewart [10–12]. In this approach,

$$\phi(x,p) = \epsilon + \epsilon_\mu p^\mu + \epsilon_{\mu\nu} p^\mu p^\nu, \tag{23}$$

where the coefficients ϵ, ϵ_μ, and $\epsilon_{\mu\nu}$ are the expansion parameters and therefore $\sim O(\mathrm{Kn})$.

For each nonequilibrium state given by f the corresponding equilibrium state f_0 is defined by the Landau matching conditions [12], such that $n_0 = n$ and $e_0 = e$. These conditions together with the Gibbs equation ensure that the equilibrium part of the pressure is given by the equation of state $p_0(e,n) = p_0(e_0,n_0)$.

The coefficients of the expansion, ϵ, ϵ_μ, and $\epsilon_{\mu\nu}$, are determined using Eq. (23) in Eqs. (2) and (3). Comparing the outcome with Eqs. (10) and (11), one finds that the parameters of the expansion are proportional to the dissipative quantities Π, V^μ, q^μ, and $\pi^{\mu\nu}$. Thus the deviation from equilibrium is proportional to the ratio of dissipative quantities to local equilibrium quantities, that is, $\phi \sim \Pi/e, q^\mu/e, \pi^{\mu\nu}/e$. However, if the dissipative quantities are close to the Navier-Stokes values (see later), then these ratios are proportional to the local Knudsen number.

The macroscopic equations for the evolution of dissipative quantities can be obtained from the third moment of the single-particle distribution function [12]. Here we recall the result of this laborious calculation by Israel and Stewart as presented by Huovinen and Molnár [14]. In this paper we consider only massless gases in which case bulk viscosity vanishes. Then the IS equations for the heat flow and the shear-stress tensor are

$$\begin{aligned} Dq^\mu = {} & \frac{1}{\tau_q}\left(q^\mu_{\mathrm{NS}} - q^\mu\right) - \omega^{\mu\lambda}q_\lambda - u^\mu q_\nu Du^\nu \\ & - \frac{1}{2}q^\mu\left(\nabla_\lambda u^\lambda + D\ln\frac{\beta_1}{T}\right) \\ & + \frac{\alpha_1}{\beta_1}(\partial_\lambda \pi^{\lambda\mu} + u^\mu \pi^{\lambda\nu}\partial_\lambda u_\nu) - \frac{a_1}{\beta_1}\pi^{\lambda\mu}Du_\lambda, \end{aligned} \tag{24}$$

$$\begin{aligned} D\pi^{\mu\nu} = {} & \frac{1}{\tau_\pi}\left(\pi^{\mu\nu}_{\mathrm{NS}} - \pi^{\mu\nu}\right) - 2\pi_\lambda^{\langle\mu}\omega^{\nu\rangle\lambda} \\ & - (\pi^{\lambda\mu}u^\nu + \pi^{\lambda\nu}u^\mu)Du_\lambda \\ & - \frac{1}{2}\pi^{\mu\nu}\left(\nabla_\lambda u^\lambda + D\ln\frac{\beta_2}{T}\right) \\ & - \frac{\alpha_1}{\beta_2}\nabla^{\langle\mu}q^{\nu\rangle} + \frac{a_1'}{\beta_2}q^{\langle\mu}Du^{\nu\rangle}, \end{aligned} \tag{25}$$

where the proper-time derivative is denoted by $D \equiv u^\mu\partial_\mu$, the gradient operator is $\nabla^\mu = \Delta^{\mu\nu}\partial_\nu$, and the vorticity tensor is $\omega^{\mu\nu} = \frac{1}{2}\Delta^{\mu\alpha}\Delta^{\beta\nu}(\partial_\beta u_\alpha - \partial_\alpha u_\beta)$. The coefficients $\alpha_1, \beta_1, \beta_2$, and a_1 are thermodynamic functions, and $a_1' = [\partial(\beta\alpha_1)/\partial\beta]_{\mu/T} - a_1$. These depend whether we choose the

Landau or Eckart frame. The Navier-Stokes values for the heat flow and shear-stress tensor are

$$q^{\mu}_{\rm NS} \equiv -\kappa_q \frac{nT^2}{e+p}\nabla^{\mu}\left(\frac{\mu}{T}\right), \tag{26}$$

$$\pi^{\mu\nu}_{\rm NS} \equiv 2\eta\nabla^{\langle\mu}u^{\nu\rangle}, \tag{27}$$

where κ_q is the heat conductivity coefficient and η is the shear viscosity coefficient. The relaxation times of heat conductivity and shear viscosity are proportional to the heat conductivity and shear viscosity coefficient, respectively, that is, $\tau_q = \kappa_q T\beta_1$ and $\tau_\pi = 2\eta\beta_2$.

The microscopic time scales in the IS equations are given by the relaxation times of dissipative quantities τ_π and τ_q, which are of the order of the mean-free path between collisions. The relevant macroscopic scales can be estimated from the gradients of the primary fluid-dynamical variables. For example, these can be given in terms of the expansion rate $L_\theta = 1/\theta$, in terms of the energy density gradient $L_e^{-1} = \sqrt{\nabla^\mu e \nabla_\mu e}/e$, or in other ways.

If the Knudsen number is sufficiently small, then at late times $t > \tau_\pi, \tau_q$, heat flow and shear viscosity will approach their Navier-Stokes values, that is, $q^\mu \sim q^\mu_{\rm NS}$ and $\pi^{\mu\nu} \sim \pi^{\mu\nu}_{\rm NS}$. When this happens, the dissipative quantities can be estimated to be of order 1 in the Knudsen number, and Eqs. (24) and (25) include contributions up to second order in Kn.

In the limit $\tau_q, \tau_\pi \to 0$, with η and κ_q constant, the IS equations reduce to the Navier-Stokes equations. Furthermore, in the limit when all dissipative quantities approach zero, the IS equations reduce to the perfect-fluid equations.

C. The Israel-Stewart equations for (1 + 1)-dimensional expansion

For the sake of simplicity, we assume an ultrarelativistic massless Boltzmann gas with conserved particle number. In this case, the bulk viscosity vanishes, and the equation of state is simply $e = c_s^{-2}p$, where the speed of sound is $c_s = \sqrt{1/3}$. For gluons, the energy density as a function of temperature is $e = 3nT$, where $n = \lambda g T^3/\pi^2$ is the number density, with $g = 16$ being the gluon number of degrees of freedom. The entropy density is given by $s = (4 - \ln\lambda)n$.

In the following we choose the Landau frame. We shall briefly discuss and write the IS equations in (1 + 1)-dimensional Cartesian coordinates. We assume that the system is homogeneous in the transverse directions x and y, and evolves along the longitudinal direction z such that the velocities as well as the derivatives in both transverse directions vanish identically. Thus the four-velocity is $u^\mu = \gamma_z(1, 0, 0, v_z)$ where $\gamma_z = (1 - v_z^2)^{-1/2}$, while the four-derivative is $\partial_\mu = (\partial_t, 0, 0, \partial_z)$. The following four-vector and tensor components vanish: $N^x = N^y = 0$ and $T^{0x} = T^{0y} = T^{xy} = T^{xz} = T^{yz} = 0$. This also implies that the heat-flow components $q^x = q^y = 0$ and shear-stress tensor components $\pi^{0x} = \pi^{0y} = \pi^{xy} = \pi^{xz} = \pi^{yz} = 0$ vanish identically.

Using the orthogonality of the heat-flow four-vector, we obtain that $q^0 = q^z v_z$. We may also define the magnitude of the heat-flow four-vector by $q = \sqrt{-q^\mu q_\mu}$; thus $q^z = \gamma_z q$. Similarly, using the orthogonality property of the shear-stress tensor we get $\pi^{00} = \pi^{0z}v_z$ and $\pi^{0z} = \pi^{zz}v_z$. To satisfy the tracelessness condition we may choose $\pi^{xx} = \pi^{yy} = -\pi/2$ and $\pi^{zz} = \gamma_z^2\pi$.

Therefore, the nonvanishing components of the particle four-current and energy-momentum tensor are

$$N^0 \equiv n\gamma_z - \frac{q^z v_z}{h}, \tag{28}$$

$$N^z \equiv N^0 v_z - \frac{q^z}{\gamma_z^2 h}, \tag{29}$$

$$T^{00} \equiv (e + \mathcal{P}_z)\gamma_z^2 - \mathcal{P}_z, \tag{30}$$

$$T^{0z} \equiv v_z(T^{00} + \mathcal{P}_z), \tag{31}$$

$$T^{xx} \equiv p - \frac{\pi}{2} = T^{yy}, \tag{32}$$

$$T^{zz} \equiv v_z T^{0z} + \mathcal{P}_z, \tag{33}$$

where the LRF effective pressure is

$$\mathcal{P}_z = p(e, n) + \pi. \tag{34}$$

The LRF particle and energy densities expressed through the laboratory frame quantities and the velocity are

$$n = N^0\left(\left(1 - v_z^2\right)^{-1/2} - \frac{q^z v_z}{e+p}\right)^{-1}, \tag{35}$$

$$e = T^{00} - v_z T^{0z} = T^{00} - \frac{(T^{0z})^2}{T^{00} + \mathcal{P}_z}, \tag{36}$$

$$v_z = \frac{T^{0z}}{T^{00} + \mathcal{P}_z}. \tag{37}$$

The conservation equations are

$$\partial_t N^0 + \partial_z(v_z N^0) = \partial_z\left(\frac{q^z n}{\gamma^2(e+p)}\right), \tag{38}$$

$$\partial_t T^{00} + \partial_z(v_z T^{00}) = -\partial_z(v_z\mathcal{P}_z), \tag{39}$$

$$\partial_t T^{0z} + \partial_z(v_z T^{0z}) = -\partial_z\mathcal{P}_z. \tag{40}$$

The relaxation equations for the heat conductivity are calculated from Eqs. (24) and (25). In the (1 + 1)-dimensional case the terms containing the vorticity vanish; therefore the relaxation equations can be written formally as

$$Dq^z = \frac{1}{\tau_q}\left(q^z_{\rm NS} - q^z\right) - I^z_{q1} - I^z_{q2} - I^z_{q3}, \tag{41}$$

$$D\pi = \frac{1}{\tau_\pi}(\pi_{\rm NS} - \pi) - I_{\pi 1} - I_{\pi 2} - I_{\pi 3}, \tag{42}$$

where the Navier-Stokes values for the heat conductivity and shear stress are

$$\pi_{\rm NS} = -\frac{4}{3}\left(\frac{\eta}{s}\right)s\theta_z, \tag{43}$$

$$q^z_{\rm NS} = \left(\frac{\kappa_q T}{s}\right)\frac{(Ts)n}{e+p}\gamma_z^2\left(v_z\frac{\partial_t\lambda}{\lambda} + \frac{\partial_z\lambda}{\lambda}\right). \tag{44}$$

The expansion rate is denoted by $\theta_z = \partial_t\gamma_z + \partial_z(\gamma_z v_z)$. In the ultrarelativistic limit, $\alpha_1 = -1/(4p)$, $\beta_1 = 5/(4p)$, $\beta_2 = 3/(4p)$, $a_1 = 0$, and $a_1' = 5\alpha_1$. The terms in the relaxation

equations are given explicitly as

$$I^z_{q1} = \frac{1}{2}q^z\left(\theta_z + D\ln\frac{\beta_1}{T}\right), \tag{45}$$

$$I^z_{q2} = -q^z v_z \gamma_z^3(\partial_t v_z + v_z\partial_z v_z), \tag{46}$$

$$I^z_{q3} = \frac{1}{5}\left[\gamma_z^2(v_z\partial_t\pi + \partial_z\pi) + \gamma_z\pi(v_z\theta_z + \gamma_z\partial_t v_z)\right], \tag{47}$$

and

$$I_{\pi 1} = \frac{1}{2}\pi\left(\theta_z + D\ln\frac{\beta_2}{T}\right), \tag{48}$$

$$I_{\pi 2} = \frac{10}{9}\left(q^z\gamma_z^2\right)(\partial_t v_z + v_z\partial_z v_z), \tag{49}$$

$$I_{\pi 3} = \frac{2}{9}\left(v_z\partial_t q^z + \partial_z q^z - \frac{q^z v_z}{\gamma_z}\theta_z\right). \tag{50}$$

The terms I^z_{q3}, $I_{\pi 2}$, and $I_{\pi 3}$ represent a coupling between the heat-flow four-vector and shear-stress tensor.

In this work the term I^z_{q3} is neglected in most cases unless otherwise stated. The reason is that the agreement with kinetic theory is better without it, but results with and without this coupling term will be shown when we discuss viscous solutions to the Riemann problem.

III. NUMERICAL METHODS

A. The transport model: BAMPS

The microscopic transport model we use is the Boltzmann approach of multiparton scatterings (BAMPS) [30,31]. This numerical method solves the Boltzmann equation (1) for on-shell particles based on the stochastic interpretation of transition rates. In this study we consider only binary collisions with an isotropic cross section, that is, a cross section with an isotropic distribution of the collision angle.

Simulations of the space-time evolution of particles are performed in a static box. Because we consider shock-wave propagation in one dimension as described in the next section, we choose the z axis as the direction along which shock waves propagate. The x and y axes span the transverse plane.

The whole box is divided into spatial cells with a volume $V_{\rm cell} = \Delta x\Delta y\Delta z$. Collisions of particles in the same cell are simulated by Monte Carlo technique according to the individual collision probability within a time step Δt,

$$P_{22} = v_{\rm rel}\frac{\sigma}{N_{\rm test}}\frac{\Delta t}{V_{\rm cell}}, \tag{51}$$

where σ is the total cross section, and $v_{\rm rel} = (p_1 + p_2)^2/(2E_1E_2)$ denotes the relative velocity of the two incoming particles with four-momenta p_1, p_2. In order to reduce statistical fluctuations in simulations and to ensure an accurate solution of the Boltzmann equation (1) a test-particle method [30] is introduced: The particle number is artificially increased by multiplying it by the number of test particles per real particle, $N_{\rm test}$. Thus, the collision probability has to be reduced by the same number to keep the particle mean-free path independent of the value of $N_{\rm test}$.

If a collision occurs, momenta of colliding particles are changed according to the isotropic distribution of the collision angle. Before and after collisions particles propagate via free streaming. Collisions of particles against box boundaries are realized as elastic collisions off a wall. We have to stop simulations before the shock front reaches the box boundaries, otherwise it would get reflected.

The relationship between the shear viscosity η and the total cross section σ is given by $\eta = 4e/(15R^{\rm tr})$ [32], where $R^{\rm tr} = n\langle v_{\rm rel}\sigma^{\rm tr}\rangle = 2n\langle v_{\rm rel}\sigma\rangle/3$ is the transport collision rate in the case of isotropic scattering processes [14]. $\langle\rangle$ stands for the ensemble average in the LRF. In IS theory, we obtain

$$\eta = \tfrac{2}{5}e\lambda_{\rm mfp} \tag{52}$$

for an ultrarelativistic massless gas, where $\lambda_{\rm mfp} = 1/(n\langle v_{\rm rel}\sigma\rangle)$ is the particle mean-free path. Note that $\langle v_{\rm rel}\sigma\rangle$ is inversely proportional to $\lambda_{\rm mfp}$ and η/s. For given constant $\lambda_{\rm mfp}$ or η/s, the average $\langle v_{\rm rel}\sigma\rangle$ in individual cells is generally different, if there exists a spatial gradient of n and/or e. In these cases we assume that σ does not depend on the momenta of two incoming particles. This leads to $\langle v_{\rm rel}\sigma\rangle \approx \sigma$, because $\langle v_{\rm rel}\rangle \approx 1$ in the LRF.

In the following, we shall also need the relationship between the heat conductivity and the cross section [19,33] which, in IS theory, is

$$\kappa_q = 2/\sigma. \tag{53}$$

B. The viscous hydro solver: vSHASTA

In order to solve the IS equations of causal relativistic fluid dynamics we use a version of the sharp and smooth transport algorithm (SHASTA) [34]. This numerical method is widely used in modeling relativistic heavy-ion collisions, and hence was extensively tested in the perfect-fluid approximation [35,36]. We apply SHASTA to solve both the conservation equations and the relaxation equations rearranged in conservation form and call this numerical method vSHASTA [37].

This algorithm requires the Courant-Friedrichs-Lewy (CFL) condition $\lambda_{\rm CFL} = \Delta t/\Delta z \leqslant 0.5$, where Δt is the time step and Δz is the cell size. In all our numerical calculations we take $\lambda_{\rm CFL} = 0.4$. In a first-order finite-difference approach this means that causal transport of matter covers only a distance $\lambda_{\rm CFL}\Delta z$, while the remaining part of the matter is acausally diffused over a distance $(1 - \lambda_{\rm CFL})\Delta z$. This purely numerical effect called prediffusion is partially removed by higher-order nonlinear corrections in SHASTA. The remaining low-order numerical diffusion represents the so-called numerical viscosity of the algorithm. In a strict sense numerical viscosity does not fully correspond to real physical viscosity, which is independent of the numerical method and resolution. However, its presence is inevitable and at the same time compulsory to keep the computations stable and to smooth out dispersion errors. By increasing the numerical resolution this numerical diffusion can always be reduced to smaller values than the physical one.

We also mention another rather trivial numerical artifact which is present in the numerical solutions at early times. The numerical solutions at early times do not represent the correct and accurate physical behavior, not even in the perfect-fluid limit. However, this will change in time as the solution spreads over a larger number of cells while the structures are resolved

on a finer grid. Therefore, the numerical solutions approach the correct solution only after some amount of time.

IV. TESTING THE PERFECT-FLUID LIMIT

A. The relativistic Riemann problem in the perfect-fluid limit

In this section we introduce the relativistic Riemann problem in the case of perfect fluids. The matter is assumed to be thermodynamically normal [38] and, for the sake of simplicity, to be homogeneous in the transverse directions, so the problem becomes $(1+1)$ dimensional.

In the Riemann problem we have matter in thermodynamical equilibrium separated by a membrane at $z=0$. The pressures on the left ($z<0$) and right ($z\geqslant 0$) sides of the membrane are p_0 and p_4, and the particle densities are n_0 and n_4, respectively. Here we only discuss a special case of the Riemann problem, called the shock-tube problem, when the velocities on both sides of the membrane are zero, that is, $v_0=v_4=0$.

Removal of the membrane at time $t=0$ leads to two propagating waves. If $p_0>p_4$, a shock wave is propagating to the right with the velocity $v_{\rm shock}$. Simultaneously, the tail of a rarefaction fan is propagating to the left with the speed of sound c_s into the matter with higher pressure. The region between these two waves includes a contact discontinuity, propagating to the right with v_3, and a shock plateau, which is bounded by the contact discontinuity and the shock front.

Figure 1 shows the analytic solution for the particle density and velocity profile for an ultrarelativistic massless gas,

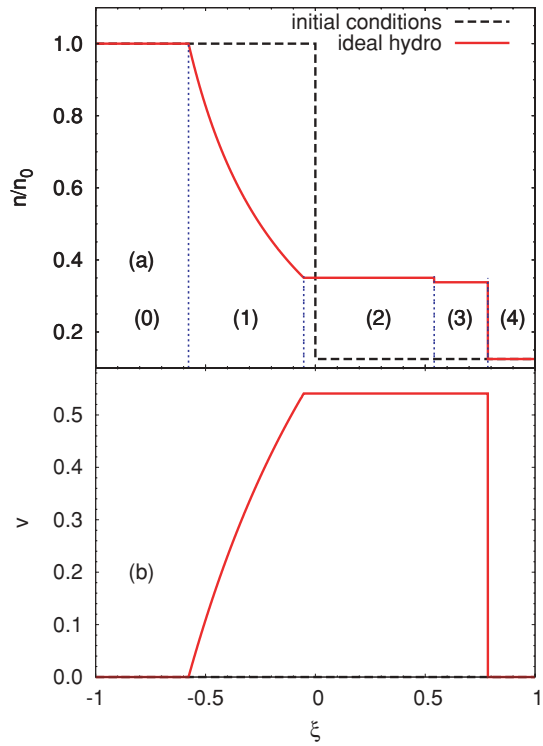

FIG. 1. (Color online) Analytic solution of the Riemann problem for a perfect fluid, (a) particle density and (b) velocity, as a function of the similarity variable $\xi=z/t$. The initial temperatures are $T_0=0.4$ GeV and $T_4=0.2$ GeV.

$e=3p$. Here, regions 0 and 4 represent the undisturbed matter at rest, 1 is the rarefaction wave, 2 denotes the constant region between the tail of the rarefaction wave and the contact discontinuity, while 3 is the shock plateau. The shock front is the discontinuity between regions 3 and 4.

The solution of the relativistic Riemann problem is obtained by matching the pressure p_2 and velocity v_2 at the rarefaction tail to the pressure and velocity of the shock plateau p_3 and v_3, that is, $p_2=p_3$ and $v_2=v_3$; see Ref. [35] for more details.

The solution at the discontinuity is given by the Rankine-Hugoniot-Taub relations [21] in the LRF of the shock,

$$\begin{aligned} n_3\widehat{u}_3 &= n_4\widehat{u}_4,\\ (e_3+p_3)\widehat{\gamma}_3\widehat{u}_3 &= (e_4+p_4)\widehat{\gamma}_4\widehat{u}_4,\\ (e_3+p_3)\widehat{u}_3^2+p_3 &= (e_4+p_4)\widehat{u}_4^2+p_4. \end{aligned} \tag{54}$$

Quantities with a caret are evaluated in the LRF of the shock. Then, the velocities of the shock plateau and the shock front in the LRF of the undisturbed matter can be expressed in terms of thermodynamic quantities before and after the discontinuity,

$$v_{\rm plat}\equiv v_3=\left(\frac{(p_3-p_4)(e_3-e_4)}{(e_4+p_3)(e_3+p_4)}\right)^{1/2}, \tag{55}$$

$$v_{\rm shock}\equiv -\widehat{v}_4=\left(\frac{(p_4-p_3)(e_3+p_4)}{(e_4-e_3)(e_4+p_3)}\right)^{1/2}, \tag{56}$$

where $e_i=3p_i$, $i=3,4$, for an ultrarelativistic gas of massless particles.

The solution for the ideal shock-tube problem is self-similar in time, that is, the solution keeps the same shape at all times, $t>0$, without change. This is best seen if we plot the solutions against the similarity variable, $\xi=z/t$, as is done in Fig. 1.

B. Numerical convergence of BAMPS

Before we employ BAMPS to solve the Riemann problem near the perfect-fluid limit in the next subsection, we first show the convergence of BAMPS when the model parameters are varied.

In BAMPS the relevant parameters that control the numerical accuracy are the cell size Δz, the time step Δt, and the test-particle number per real particle, $N_{\rm test}$. The cell sizes in the transverse directions, Δx and Δy, are not relevant, because the system is assumed to be homogeneous in the transverse plane. In addition, Δt is always chosen to be smaller than Δz, to avoid possible large local variations within one time step. If one decreases Δz, one has to simultaneously increase $N_{\rm test}$ to ensure that each cell contains a sufficiently large number of test particles. Thus, using BAMPS the Boltzmann equation (1) will be exactly solved in the limit $\Delta z\to 0$ and $N_{\rm test}\to\infty$. In practice we of course use a nonvanishing value of Δz and a finite value of $N_{\rm test}$. In the following we show how the numerical solutions converge when Δz is decreased and $N_{\rm test}$ is increased.

The initial condition for this study is $T_0=0.4$ GeV and $T_4=0.35$ GeV. Figure 2 shows the pressure profile at a time $t=3.2$ fm/c for a constant mean-free path $\lambda_{\rm mfp}=0.1$ fm. Results in the upper panel are obtained by varying Δz and keeping $N_{\rm test}$ unchanged. The number of test particles in the

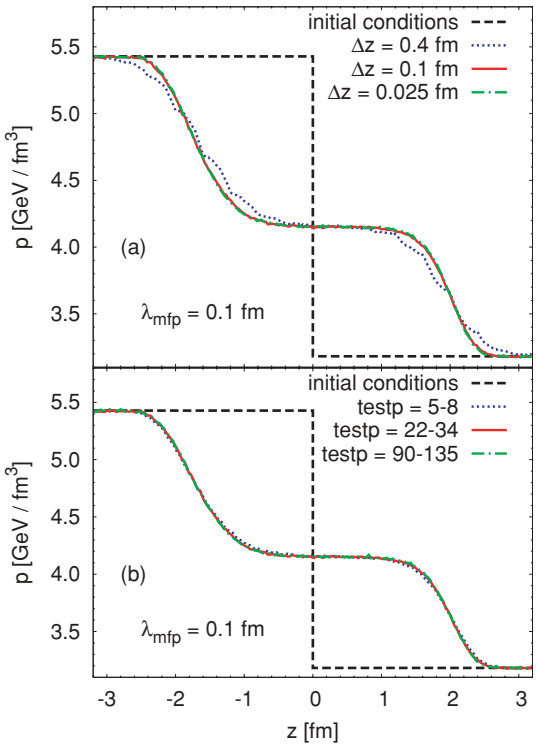

FIG. 2. (Color online) Cell size (a) and number of test particle (b) dependence in the BAMPS simulation at $t = 3.2$ fm/c. The initial conditions are chosen as $T_0 = 0.4$ GeV and $T_4 = 0.35$ GeV. The mean-free path is $\lambda_{\text{mfp}} = 0.1$ fm. In (a) the pressure profile is shown for different cell size $\Delta z = 0.4, 0.1, 0.025$ fm and constant N_{test}. In (b) we use a fixed $\Delta z = 0.1$ fm and different numbers of test particles (testp) per cell.

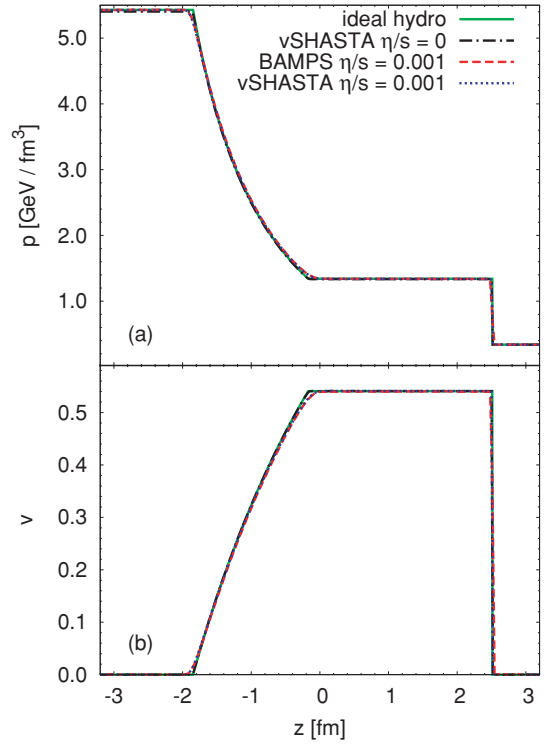

FIG. 3. (Color online) The analytic and numerical solutions of the relativistic Riemann problem for the pressure (a) and velocity (b). The initial conditions at $t = 0$ are $T_0 = 0.4$ GeV and $T_4 = 0.2$ GeV. The full lines are the analytic solutions at $t = 3.2$ fm/c. The results from BAMPS for $\eta/s = 0.001$ are shown with dashed lines, the vSHASTA results in the perfect-fluid limit with dash-dotted lines, and those for $\eta/s = 0.001$ with dotted lines.

cells is between 22 and 34, depending on the local temperature. We see that convergence is reached when $\Delta z = \lambda_{\text{mfp}}$. Further decrease of Δz does not lead to noticeable changes. The lower panel of Fig. 2 shows the results for a fixed Δz and varying number of test particles per cell. Here we do not see significant changes even for a small test-particle number in the cells. However, as we will show in the next subsection, a small number of testparticles in cells causes large fluctuations in each event, and thus affects heat flow, for instance.

Results from BAMPS, which will be presented in the rest of the paper, are obtained by setting $\Delta z \leqslant \lambda_{\text{mfp}}$ and taking at least 15 test particles in each cell. We note that for these calculations a different initial condition, $T_0 = 0.4$ GeV and $T_4 = 0.2$ GeV, is chosen. For this case a faster convergence has been observed.

C. Numerical solutions of the relativistic Riemann problem near the perfect-fluid limit

The Riemann problem, which is analytically solvable in the perfect-fluid limit, is an important test case for both the kinetic and the fluid-dynamical calculations. In this section we show that both approaches can reproduce the analytic solution very accurately, and also discuss possible numerical uncertainties.

In BAMPS we cannot exactly reach the perfect-fluid limit, but we can choose a very small physical viscosity $\eta = 0.001s$ to simulate an ideal fluid numerically. Use of even smaller viscosities, or equivalently larger cross sections, would require a better resolution (smaller Δz and larger N_{test}), which is computationally very time consuming.

On the other hand, for vSHASTA we can choose $\eta = \kappa_q = 0$, which solves the relativistic Euler equations instead of the IS equations. However, as explained earlier, because of the approximative nature of the numerical algorithm, we always have some residual numerical viscosity in the calculations.

In both calculations the initial state was chosen such that $T_0 = 0.4$ GeV and $T_4 = 0.2$ GeV. Figure 3 shows the pressure p and velocity v, while Fig. 4 shows the LRF particle density n and fugacity λ profiles at time $t = 3.2$ fm/c.

The BAMPS results for p, v, and n agree well with those of the ideal fluid-dynamical solution, except for small deviations around the discontinuities separating different regions. These deviations are expected to appear because of the small but nonvanishing physical viscosity used in BAMPS calculations, and are best seen in the fugacity profile.

Nevertheless, the BAMPS results also deviate from vSHASTA using the same η/s value; this is especially visible in the fugacity profile between the contact discontinuity and the shock front, where one observes a peak in the BAMPS result. We will demonstrate later that this deviation is caused by numerical fluctuations.

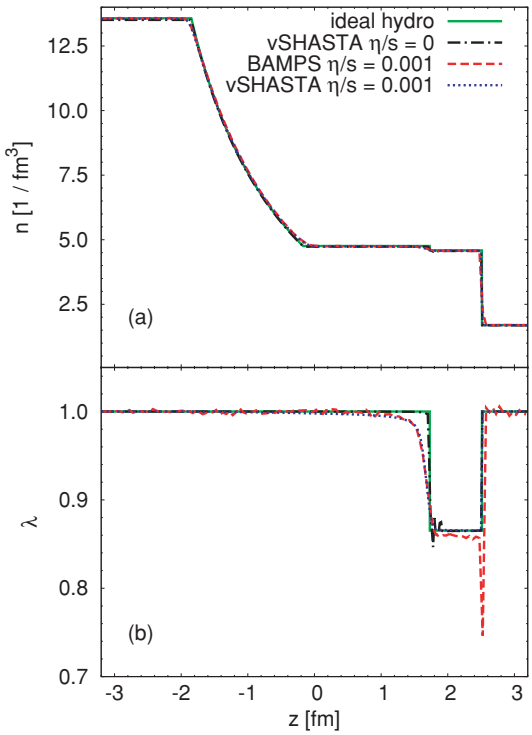

FIG. 4. (Color online) Same as in Fig. 3. The upper panel (a) shows the particle density while the lower panel (b) shows the fugacity.

We also expect that particles in regions around discontinuities are out of thermal equilibrium in the BAMPS calculations. However, this is a small fraction of the whole system. The rest reaches and approximately maintains thermal equilibrium. In order to demonstrate this, we calculate the energy distribution $dN/(NdE)$ of particles in the region of the shock plateau and compare it to the thermal one, which is obtained by using Eq. (22) with $a = 0$,

$$\frac{dN}{NdE} = \frac{e^{-\gamma E/T}\sinh(v\gamma E/T)E}{2T^2\gamma^2 v}. \tag{57}$$

Results are shown in Fig. 5, where we see agreement within a few percent.

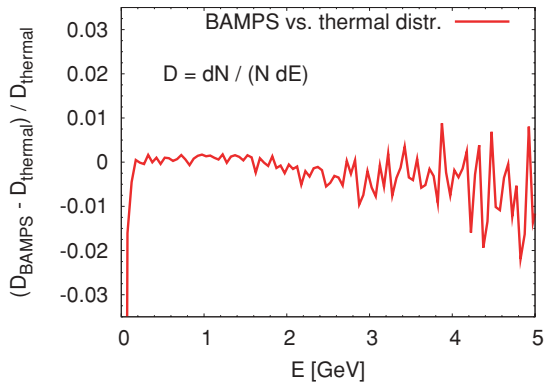

FIG. 5. (Color online) Relative difference of energy distribution of particles at the plateau extracted from BAMPS and a local thermal equilibrium distribution, Eq. (57).

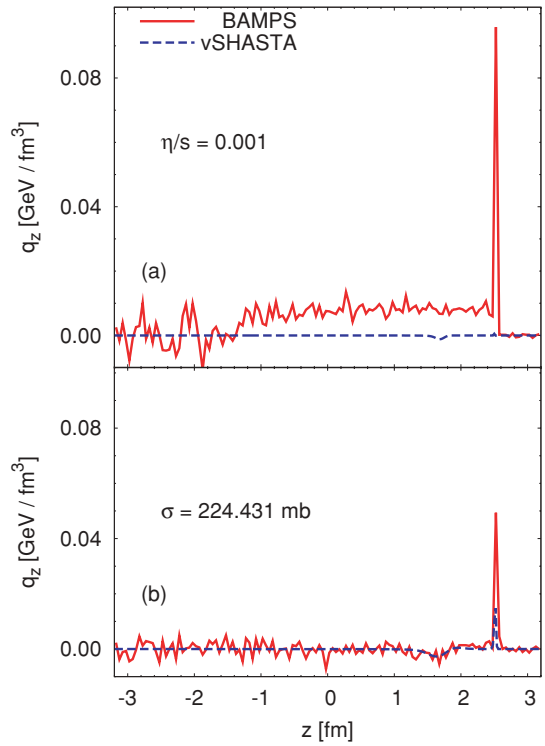

FIG. 6. (Color online) The heat-flow component (a) with fixed $\eta/s = 0.001$ and (b) with constant cross section $\sigma = 224.431$ mb. The value of η/s in the constant cross section simulation varies from 0.002 to 0.008.

If the system is exactly in thermal equilibrium as described by the ideal fluid-dynamical solution, the dissipative quantities, such as the heat flow q^z, should vanish. Figure 6(a) shows the heat-flow profiles from both vSHASTA and BAMPS calculations with the same initial condition with $\eta/s = 0.001$. Heat flow in vSHASTA is practically zero, while in BAMPS it has a small positive value between the rarefaction fan and the shock front. This deviation between BAMPS and vSHASTA results was already noticeable in the fugacity profile, but not in the other quantities shown above. At the shock front we see a peak, similar as for the fugacity profile.

The deviation of q^z from zero observed in Fig. 6(a) (except for the peak) seems to be a numerical artifact, because this disappears when a constant cross section is used instead of a constant η/s value, as shown in Fig. 6(b). Here, the cross section is set to be $\sigma = 224.431$ mb, which corresponds to $\eta/s = 0.002$ in the medium with the higher initial temperature. In Fig. 6(b) we see perfect agreement between BAMPS and vSHASTA results, especially comparing them at the small drop at $z \approx 1.6$ fm. The peak at the shock front becomes smaller, although it is larger than the peak from the vSHASTA calculation.

Also, the difference in the fugacity between BAMPS and vSHASTA with the same η/s value, as observed in the lower panel of Fig. 4, disappears almost completely when using a constant cross section, as seen in Fig. 7.

On the shock plateau where the flow velocity and the LRF particle and energy density (v,n,e) are constant, one expects that the cross section is also constant for a constant

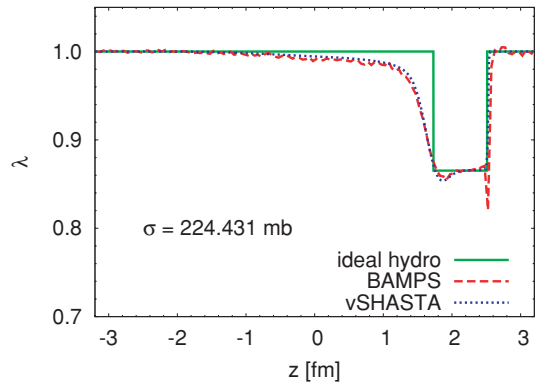

FIG. 7. (Color online) Fugacity calculated using a constant cross section $\sigma = 224.431$ mb.

η/s. However, in a single event, thermodynamic quantities fluctuate, such that one would use a smaller cross section (larger shear viscosity) in a cell with larger energy (entropy) density in order to keep η/s constant, and a larger cross section in a cell with smaller energy density. Therefore, although the results shown in Figs. 4 (lower panel) and 6(a) are averaged over 1000 events, the deviations between BAMPS and vSHASTA results are likely to come from the fluctuations in single BAMPS events. These can be reduced by performing simulations with a much larger N_{test}. We have confirmed that in this case the difference between BAMPS and vSHASTA solutions decreases.

V. VISCOUS SOLUTIONS OF THE RELATIVISTIC RIEMANN PROBLEM

In this section we study the relativistic Riemann problem at different nonzero viscosities. We will show that for small viscosities both the fluid-dynamical and kinetic approaches are in good agreement, especially at late times. However, with increasing viscosity this agreement fades and ultimately breaks down when the fluid-dynamical description leads to results which are inconsistent with kinetic calculations. Thus the main motivation of this study is to find the conditions of this breakdown and then quantify the reach and limits of the dissipative fluid-dynamical description.

We note that all results shown below are calculated using the Landau frame. In these test cases heat flow is small; therefore the differences between the Landau or Eckart frames are very small, even for large values of η/s.

Kinetic theory can correctly treat the Riemann problem from the nearly perfect limit to the free-streaming limit. This has been previously demonstrated in Refs. [16,17] using BAMPS. Another promising method to investigate the Riemann problem is based on the lattice Boltzmann approach and has been recently reported in Ref. [39]. In contrast to kinetic theory, the validity of IS theory requires that the system stays close to local thermal equilibrium and the Knudsen number Kn is small during the whole evolution.

In the special case of the Riemann problem, at early times of the evolution, the local Knudsen number is large where the density gradients are large, even if the viscosity is small. Also the system around the discontinuity is far from equilibrium. Then in this region the IS theory of dissipative fluid dynamics is expected to fail to describe the evolution correctly.

However, because of the viscosity and heat conductivity the gradients will be smoothed out later, hence providing better conditions for the IS fluid-dynamical description. How close the solution will be to the kinetic one depends on the value of the Knudsen number as demonstrated later in Sec. V D.

In the next subsections we will show results at fixed times but for different values of η/s. However, solutions at time t with shear viscous coefficient η correspond to solutions at time at with shear viscous coefficient $a\eta$, where a is some arbitrary constant. This scaling behavior is discussed later in Sec. VI.

A. Small viscosity

We use the same initial conditions as given in the previous section, but now for two different values of the shear viscosity to entropy density ratio, $\eta/s = 0.01$ and $\eta/s = 0.1$. Figure 8 shows the pressure p and velocity v, Fig. 9 shows the LRF particle density n and the fugacity λ, and Fig. 10 shows the profiles of the shear pressure π and the heat flux q^z at time $t = 3.2$ fm/c from both BAMPS and vSHASTA calculations.

In the dissipative case the characteristic structures of the perfect-fluid solution can still be found in the late stages of the evolution, since it takes a finite time for the structures to form; see Sec. VI. However, instead of a discontinuous shock front, a contact discontinuity, and sharp rarefaction tails, we get continuously changing profiles, that is, dissipation leads to the smoothing and broadening of these characteristic structures.

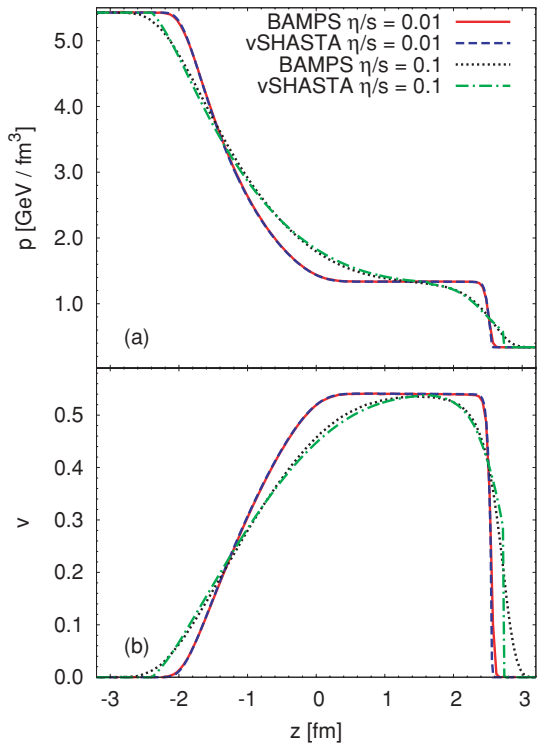

FIG. 8. (Color online) The same as Fig. 3, for $\eta/s = 0.01$ and 0.1.

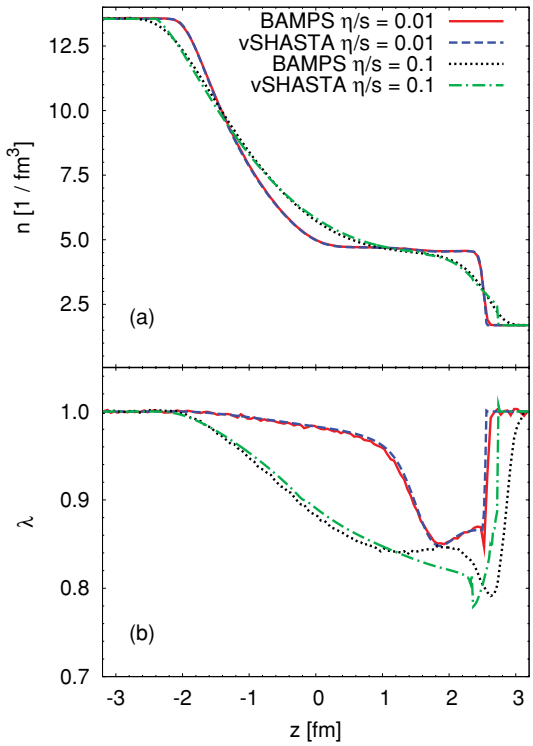

FIG. 9. (Color online) The same as Fig. 8, for (a) particle density and (b) fugacity.

Further differences compared to the perfect-fluid case are that the head and the tail of the rarefaction fan and the shock front propagate faster into the undisturbed matter. However, for the shock wave this happens only until the shock plateau is formed. After that the velocity of the shock wave is the same as for the perfect-fluid case. Similarly, the velocity of the plateau does not change from the perfect-fluid solution.

For the smaller shear viscosity to entropy density ratio, $\eta/s = 0.01$, the agreement between BAMPS and vSHASTA results for all macroscopic quantities is excellent within statistical fluctuations, although any definite conclusions regarding the heat fluxes are hard to draw because of large fluctuations. The shock front from both calculations is also in very good agreement. However, a closer inspection reveals that vSHASTA gives slightly steeper profiles than BAMPS.

Increasing the viscosity to $\eta/s = 0.1$ leads to noticeable differences between the approaches. The most pronounced difference can be seen in the shock front: vSHASTA provides a too sharp profile at the right edge of the front, while in the BAMPS calculation the matter is diffused faster in the low-density region. This can also be seen in the rarefaction fan where the kink at the left edge survives. Another difference can be seen by inspecting the fugacity and shear pressure in the region where the contact discontinuity would be in the perfect-fluid case. In this region the vSHASTA calculation returns an overall smaller fugacity, and also a sharp kink in the shear pressure profile. These differences will be enhanced for larger viscosities as seen in the next subsection.

B. Large viscosity

If the value of η/s is further increased, that is, $\eta/s = 0.2$, we start to see much larger deviations between vSHASTA and BAMPS results. These are presented in Fig. 11 for the pressure and velocity profiles.

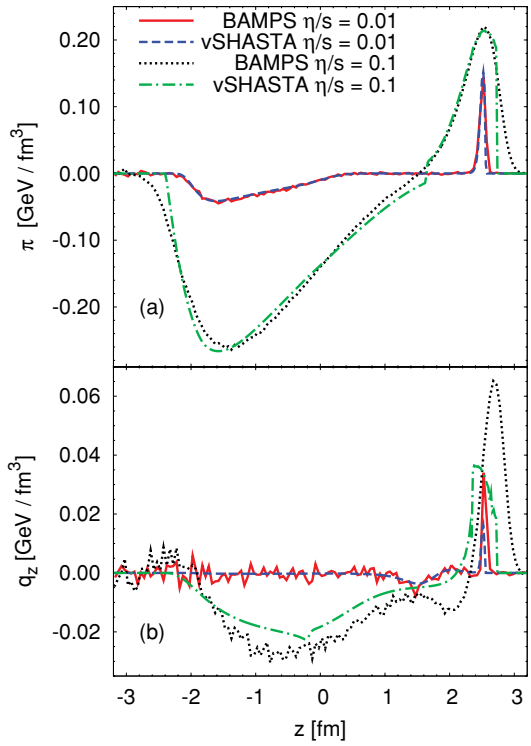

FIG. 10. (Color online) The same as Fig. 8, for (a) shear pressure and (b) heat flow.

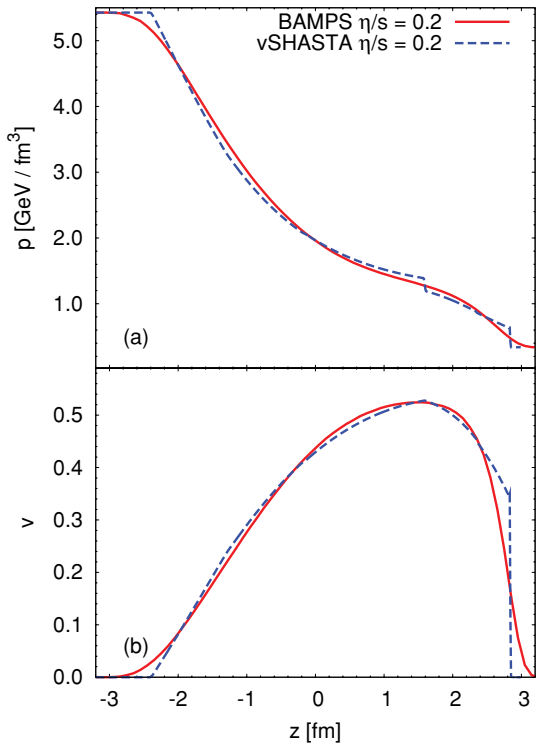

FIG. 11. (Color online) The same as Fig. 8, for $\eta/s = 0.2$.

The most salient difference is seen in the pressure profile: in the vSHASTA calculation a part of the initial discontinuity survives near the contact discontinuity, at $z \sim 1.5$ fm even after $t = 3.2$ fm/c. In contrast, this kind of structure is not seen in the BAMPS calculation. A similar shock structure was also observed in Ref. [40], called the "double-shock" phenomenon by the authors. It is important to note that in that case a different numerical method, namely, the smoothed particle hydrodynamics, was used to solve the equations of dissipative fluid dynamics, corresponding to the simplified IS equations without heat conductivity. The simplified or truncated IS equations only take into account the relaxation term to describe the time evolution of dissipative quantities.

In the fluid-dynamical calculation this discontinuity originates from the initial discontinuity. In the early stage of the evolution the effective pressure $p + \pi$ and velocity take almost constant values near the discontinuity. The velocity and the gradient of the effective pressure are the driving forces of the expansion. Therefore, if they are constant, nothing happens to the structures in the solution and the original discontinuity disappears very slowly, such that parts of it are still visible in the later stages of the evolution.

A similar difference between the BAMPS and vSHASTA results is seen at the right edge of the shock wave. This part of the profile is again not described correctly by IS fluid dynamics, and the difference is already visible for smaller values of η/s. The same is true also for the head of the rarefaction fan, although it is less visible for small viscosities. This kind of discontinuous behavior can be seen in all relevant fluid-dynamical quantities.

In the BAMPS calculation the original discontinuity disappears immediately. This is because in kinetic theory the evolution near the very steep density gradient is well approximated by free streaming or diffusion of particles, which smooths out all sharp structures very rapidly. Free streaming of particles drives the system immediately far out of thermal equilibrium, hence cannot be correctly described by second-order dissipative fluid dynamics.

This phenomena was studied and explained in nonrelativistic systems M. Torrilhon *et al.* [41]. They concluded that the viscous fluid-dynamical solutions of the Riemann problem actually lead to discontinuous solutions. For example, in the nonrelativistic 13-field equations the system has five instead of three characteristic waves. Although dissipation leads to the attenuation of these waves and smoothing of discontinuities, this can only happen after a sufficiently long time. In case we include higher moments of the distribution function we will find more characteristics and therefore more discontinuities but with smaller amplitude. There is an infinite number of moments, which form a hierarchy of equations. Therefore by taking into account higher moments the approximations to the Boltzmann equation become more precise, which in turn leads to a better approximation for smooth profiles. On this account we note that there are more recent studies showing that with a special regularization technique the Grad's 13-moment method leads to much better results [42]. So far these methods have been studied only in the nonrelativistic case, but nevertheless they point toward a solution.

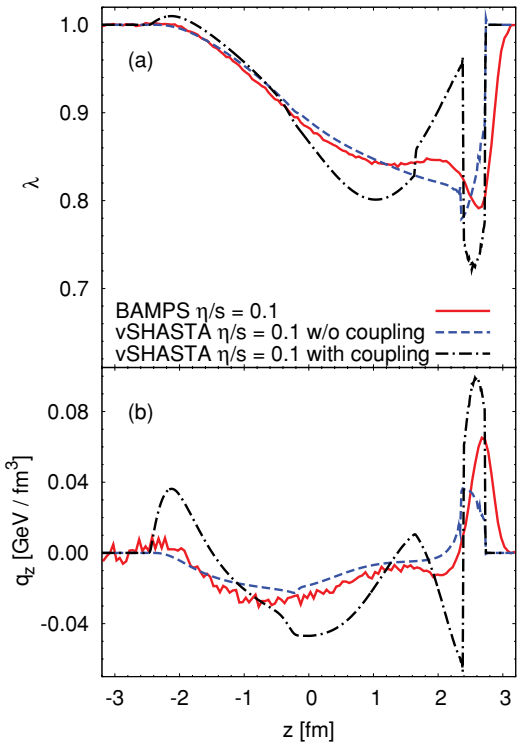

FIG. 12. (Color online) The fugacity (a) and heat-flow (b) profiles with and without coupling to the shear pressure in the heat-flow equation, I^z_{q3} in Eq. (41).

C. Heat-flow problem

As already mentioned in Sec. II C we neglected the term that couples the heat flux to the shear pressure from the heat-flow equation (41). The reason is that, if this term is included, the good agreement of heat flow and fugacity between BAMPS and vSHASTA is lost even for small viscosity. This is demonstrated in Fig. 12, where we show the fugacity λ and heat flux q^z for $\eta/s = 0.1$ with and without this coupling term. The profiles change completely, and there is no support from BAMPS for structures induced by the coupling. For other quantities this coupling term has a very small effect.

The reason that this single term can become dominant is that in the viscous Riemann problem, the heat flow is typically one order of magnitude smaller than the shear pressure. Thus, the coupling term in the heat equation can be large when the shear pressure is large, even if it is formally only a second-order correction.

D. Global Knudsen number analysis

In order to better quantify and measure the applicability of IS theory, we define the relative difference between the BAMPS and vSHASTA calculations as

$$\left\langle \frac{\delta e}{e} \right\rangle^2 = \frac{1}{\Delta z} \int dz \left(\frac{\delta e}{e} \right)^2 , \tag{58}$$

where δe is the difference in energy density between the BAMPS and the vSHASTA calculations. We recall that $e = 3p$

for a massless gas. The integral is evaluated from the head of the rarefaction fan to the tail of the shock wave; hence the constant temperature regions to the left and right are not included. The width of this region is denoted as Δz. Similarly, the average macroscopic length scale can be estimated from the average energy density gradient as

$$L_e^{-1} = \left| \frac{1}{\Delta z} \int \frac{1}{e} \frac{\partial e}{\partial z} dz \right| = \frac{1}{\Delta z} \ln \frac{e_0}{e_4}, \tag{59}$$

where e_0 and e_4 are the initial energy densities on the left- and right-hand sides of the initial discontinuity. Hence, an average Knudsen number relevant for this study can be defined as

$$\mathrm{Kn}_e = \frac{\lambda_{\mathrm{mfp}}}{L_e}, \tag{60}$$

where λ_{mfp} is the mean-free path in the low-temperature region, that is, it is the largest mean-free path. This definition smooths the rapid changes compared to a local Knudsen number and makes the comparisons between calculations feasible. Note that the Knudsen number (60) is similar to that introduced in Ref. [16].

Since $\lambda_{\mathrm{mfp}} \sim \eta/(Ts)$ and $L_e \sim t$, where t is a given time during the evolution, we also have

$$\mathrm{Kn}_e \sim \frac{\eta}{s} \frac{1}{Tt}. \tag{61}$$

Therefore, for a given temperature, Kn_e stays constant if we scale η/s and t by the same factor.

Figure 13 shows the time evolution of the average Knudsen number for two different initial conditions and two different viscosities. In all cases the Knudsen number is initially large but decreases rapidly as the system expands. This happens as a function of the initial temperature difference and viscosity.

On the other hand, the relative difference between BAMPS and vSHASTA calculations decreases with decreasing average Knudsen number. This is shown in Fig. 14 where we can see that for small Knudsen numbers the different solutions converge to approximately one curve. This also means that to good approximation the Knudsen number alone determines

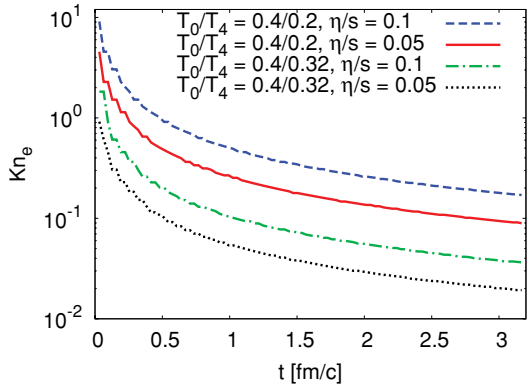

FIG. 13. (Color online) Time evolution of the average Knudsen number Kn_e for different initial temperature ratios and different values of η/s.

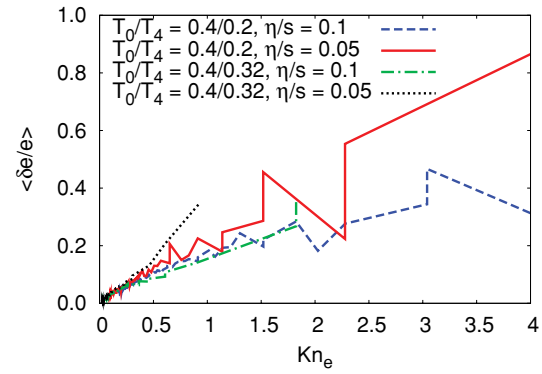

FIG. 14. (Color online) The relative difference of kinetic and fluid-dynamical calculations for different initial temperature ratios and different values of η/s as a function of the average Knudsen number.

the applicability of IS theory. We read off Fig. 14 that the differences between BAMPS and vSHASTA are less than 10% for $\mathrm{Kn}_e < 1/2$.

VI. FORMATION OF SHOCK WAVES AND THEIR SCALING BEHAVIOR

In ideal fluid dynamics shock waves are formed immediately after removing the membrane that separates matter with different temperatures. This happens because the Knudsen number Kn_e vanishes at any time. For nonvanishing viscosity Kn_e is large at early times and, thus, the formation of shock waves occurs later, when Kn_e becomes smaller, for example, in the case for a constant η/s value, as demonstrated in Fig. 13.

Figure 15 shows the pressure and velocity profiles at various times for $\eta/s = 0.1$. At the early time $t = 0.64$ fm/c shock waves have not yet developed. The pressure profile looks like that in the strong diffusive case of free-streaming particles. At $t = 6.4$ fm/c we observe a characteristic shock plateau that clearly separates the shock front from the rarefaction wave, as in the ideal-fluid case. The intermediate time $t = 3.2$ fm/c is the time scale at which the shock plateau is being formed and the maximum of the velocity distribution $v(z)$ reaches the value v_{plat} of the ideal-fluid solution. We define this time scale as the formation time of shocks.

The only intrinsic length scale in the microscopic approach is the particle mean-free path. Therefore, if we rescale the mean-free path by a constant factor of a, we expect the time scale for the evolution of matter to change accordingly. Since $\eta/s \sim \lambda_{\mathrm{mfp}}$, we expect that profiles calculated at time t for a given value of η/s agree with those at a time at for a viscosity to entropy density ratio $a\eta/s$. This is demonstrated in Fig. 16 where we show the velocity profiles as a function of the similarity variable $\xi = z/t$.

The pressure and the velocity profile as a function of ξ are determined by the Knudsen number Kn_e (60). According to Eq. (61), Kn_e is the same for the calculation with $\eta/s = 0.1$ at $t = 3.2$ fm/c and that with $\eta/s = 0.05$ at $t = 1.6$ fm/c. Therefore, the pressure $p(z, t; \eta/s)/p_0$ and

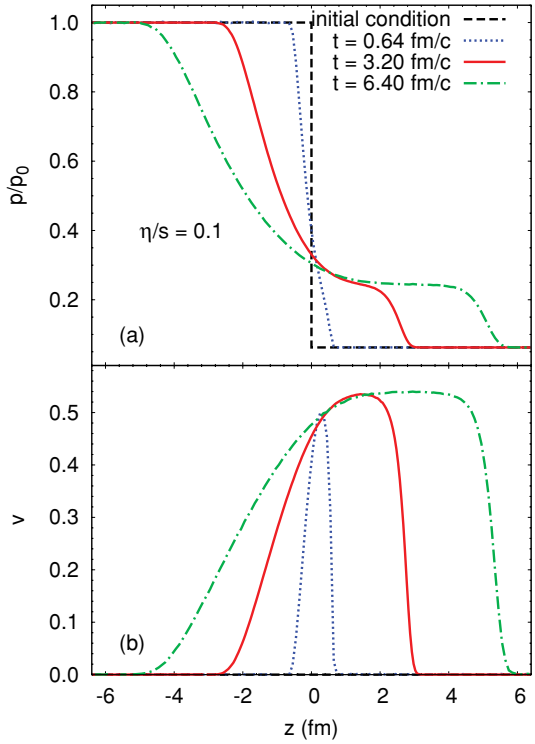

FIG. 15. (Color online) The time evolution of the shock-tube problem for $\eta/s = 0.1$. The initial condition is the same as in Fig. 3.

velocity $v(z, t; \eta/s)$ are functions only of ξ and Kn_e, that is, $p(z, t; \eta/s)/p_0 = F(\xi; \mathrm{Kn}_e)$, and similarly for the velocity. For decreasing Kn_e the plateau of the velocity profile in Fig. 16 will be growing and approaches the shape of the ideal-fluid case shown in the lower panel of Fig. 1.

This scaling behavior holds only for initial conditions with a discontinuity in pressure. If the discontinuity is changed to a smooth transition, the nonzero width Γ_{tr} of the transition region introduces another length scale. Then, as a function of the similarity variable, this transition region would change under a rescaling $t \to at$, $\xi_{\mathrm{tr}} = \Gamma_{\mathrm{tr}}/t \to \Gamma_{\mathrm{tr}}/(at)$, and thus cause a different gradient in the transition region as a function

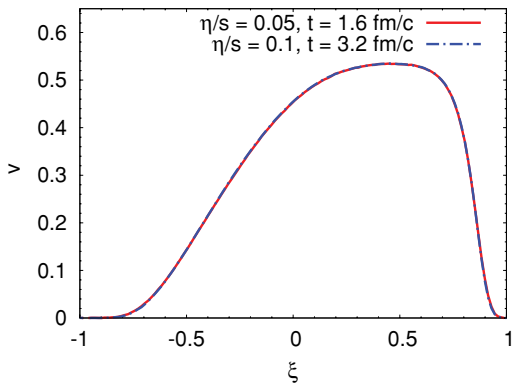

FIG. 16. (Color online) The scaling behavior for the shock-tube problem. The velocity profiles are shown as a function of the similarity variable $\xi = z/t$ for $\eta/s = 0.1$ and $\eta/s = 0.05$ at times $t = 3.2$ fm/c and $t = 1.6$ fm/c, respectively.

of ξ. Because of the different initial situations, evolutions in ξ for the same Kn_e are not identical.

VII. CONCLUSIONS

In this work we have studied the formation and evolution of relativistic shock waves in dissipative matter with nonzero shear viscosity and heat conductivity by solving the relativistic Riemann problem. This was accomplished by using both relativistic kinetic theory and relativistic dissipative fluid dynamics. The relativistic kinetic approach solves the Boltzmann equation by using the BAMPS code [30]. The fluid-dynamical approach is based on Israel and Stewart theory [12] and was solved numerically by the vSHASTA method for hyperbolic equations.

After extensive comparisons between the two approaches, we found the following: When the viscosity is zero, both give equivalent results. It was demonstrated that both approaches reproduce the analytic solutions of the Riemann problem in the perfect-fluid limit and the numerical results converge when the numerical resolution is sufficiently high.

Departing from the perfect-fluid limit, for cases when the viscosity is small, the agreement between kinetic theory and IS theory is still excellent. As the viscosity increases the agreement between the approaches starts to deteriorate. For even larger values of the η/s ratio, IS theory develops discontinuities which survive even after long times. These substructures are not supported by the kinetic simulations. They are an artifact of the method of moments [41] on which IS theory is based. However, we also argued that part of this discrepancy can be understood to result from the inapplicability of IS theory for large Knudsen numbers.

Quantitative statements about the applicability of IS theory are difficult to make in the current setup, mainly because the early evolution is not well described by fluid dynamics. This also affects the late evolution of the system, and therefore it is difficult to clearly separate between the artifacts from the early fluid-dynamical solutions and the effects of large Knudsen number.

However, we showed that a quantitative analysis in terms of an average Knudsen number is possible in such a way that it gives a good measure for the applicability of the IS theory. In accordance with Ref. [14] we found that for $\mathrm{Kn}_e < 1/2$ the difference between kinetic theory and IS theory is less than $\sim$10%.

The shear pressure profile was reasonably well described by the IS equations from small to moderate viscosities. Furthermore, we also found that the results are quite insensitive to the second-order terms in the IS equation for the shear viscosity. However, the same is not true for heat flow. At very small viscosities the heat flow was quite well described, including all terms in the IS equation. At larger viscosity the results are very sensitive to the coupling term between the heat flow and shear viscosity. In the Riemann problem studied here, the heat flow is an order of magnitude smaller than the shear pressure, and the coupling to shear dominates the behavior of the heat flow. This coupling gives a too large contribution in the heat-flow component, which is not supported by the kinetic calculations. Whether the inclusion of all second-order terms

in the IS equations will cure the heat-flow problem and improve the overall applicability of the fluid-dynamical approach will be studied in the future.

ACKNOWLEDGMENTS

The authors are grateful to P. Huovinen, G. Denicol, B. Betz, L. P. Csernai, J. A. Maruhn, and H. Stöcker for discussions and to the Center for Scientific Computing (CSC) at Frankfurt University for the computing resources. I.B. is grateful to HGS-Hire. E.M. acknowledges support by OTKA/NKTH 81655 and the Alexander von Humboldt foundation. The work of H.N. was supported by the Extreme Matter Institute (EMMI). This work was supported by the Helmholtz International Center for FAIR within the framework of the LOEWE program launched by the State of Hesse.

[1] S. S. Adler *et al.* (PHENIX Collaboration), Phys. Rev. Lett. **91**, 182301 (2003); J. Adams *et al.* (STAR Collaboration), *ibid.* **92**, 052302 (2004); B. B. Back *et al.* (PHOBOS Collaboration), Phys. Rev. C **72**, 051901 (2005).
[2] P. Kolb and U. W. Heinz, in *Quark-Gluon Plasma 3*, edited by R. C. Hwa and X. N. Wang (World Scientific, Singapore, 2004).
[3] P. Huovinen, in *Quark-Gluon Plasma 3* Ref. [2].
[4] P. Huovinen and P. V. Ruuskanen, Annu. Rev. Nucl. Part. Sci. **56**, 163 (2006).
[5] P. Danielewicz and M. Gyulassy, Phys. Rev. D **31**, 53 (1985).
[6] P. K. Kovtun, D. T. Son, and A. O. Starinets, Phys. Rev. Lett. **94**, 111601 (2005).
[7] L. P. Csernai, J. I. Kapusta, and L. D. McLerran, Phys. Rev. Lett. **97**, 152303 (2006).
[8] M. Luzum and P. Romatschke, Phys. Rev. C **78**, 034915 (2008); H. Song and U. W. Heinz, J. Phys. G **36**, 064033 (2009).
[9] Z. Xu, C. Greiner, and H. Stöcker, Phys. Rev. Lett. **101**, 082302 (2008); Z. Xu and C. Greiner, Phys. Rev. C **79**, 014904 (2009); **81**, 054901 (2010).
[10] J. M. Stewart, *Lecture Notes in Physics* (Springer-Verlag, Berlin, 1971), Vol. 10.
[11] J. M. Stewart, Proc. R. Soc. London, Ser. A **357**, 59 (1977).
[12] W. Israel and J. M. Stewart, Proc. R. Soc. London, Ser. A **365**, 43 (1979); Ann. Phys. **118**, 341 (1979).
[13] J. D. Bjorken, Phys. Rev. D **27**, 140 (1983).
[14] P. Huovinen and D. Molnar, Phys. Rev. C **79**, 014906 (2009).
[15] A. El, Z. Xu, and C. Greiner, Phys. Rev. C **81**, 041901 (2010).
[16] I. Bouras *et al.*, Phys. Rev. Lett. **103**, 032301 (2009).
[17] I. Bouras, A. El, O. Fochler, C. Greiner, E. Molnar, H. Niemi, and Z. Xu, Acta Phys. Pol. B **40**, 973 (2009); I. Bouras *et al.*, Nucl. Phys. A **830**, 741C (2009).
[18] I. Bouras *et al.*, J. Phys. Conf. Ser. **230**, 012045 (2010).
[19] S. R. de Groot, W. A. van Leeuwen, and Ch. G. van Weert, *Relativistic Kinetic Theory* (North-Holland, Amsterdam, 1980).
[20] C. Cercignani and G. M. Kremer, *The Relativisitic Boltzmann Equation: Theory and Applications* (Birkhäuser, Basel, 2002).
[21] A. H. Taub, Phys. Rev. **74**, 328 (1948).
[22] C. Eckart, Phys. Rev. **58**, 919 (1940).
[23] L. D. Landau and E. M. Lifshitz, *Fluid Dynamics*, 2nd ed. (Butterworth-Heinemann, London, 1987).
[24] W. Israel, Ann. Phys. **100**, 310 (1976).
[25] W. A. Hiscock and L. Lindblom, Ann. Phys. **151**, 466 (1983).
[26] W. A. Hiscock and L. Lindblom, Phys. Rev. D **31**, 725 (1985).
[27] S. Pu, T. Koide, and D. H. Rischke, Phys. Rev. D **81**, 114039 (2010).
[28] G. S. Denicol, T. Koide, and D. H. Rischke, arXiv:1004.5013 [nucl-th].
[29] H. Grad, Commun. Pure Appl. Math. **2**, 331 (1949).
[30] Z. Xu and C. Greiner, Phys. Rev. C **71**, 064901 (2005).
[31] Z. Xu and C. Greiner, Phys. Rev. C **76**, 024911 (2007).
[32] Z. Xu and C. Greiner, Phys. Rev. Lett. **100**, 172301 (2008).
[33] D. Molnar, arXiv:0707.1251 [nucl-th].
[34] J. P. Boris and D. L. Book, J. Comput. Phys. **11**, 38 (1973).
[35] V. Schneider *et al.*, J. Comput. Phys. **105**, 92 (1993)
[36] D. H. Rischke, S. Bernard, and J. A. Maruhn, Nucl. Phys. A **595**, 346 (1995)
[37] E. Molnar, Eur. Phys. J. C **60**, 413 (2009); E. Molnar, H. Niemi, and D. H. Rischke, *ibid.* **65**, 615 (2010).
[38] D. H. Rischke, Y. Pursun, and J. A. Maruhn, Nucl. Phys. A **595**, 383 (1995); [Erratum-*ibid.* **596**, 717 (1996)].
[39] M. Mendoza, B. M. Boghosian, H. J. Herrmann, and S. Succi, Phys. Rev. Lett. **105**, 014502 (2010).
[40] G. S. Denicol, T. Kodama, T. Koide, and Ph. Mota, Phys. Rev. C **78**, 034901 (2008).
[41] M. Torrilhon, Continuum Mech. Thermodyn. **12**, 289 (2000); J. D. Au, D. Reitebuch, M. Torrilhon, and W. Weiss, in *Proceedings of the Eighth International Conference on Hyperbolic Problems in Magdeburg, Germany 2000*, edited by H. Freistuhler and G. Warnecke, International Series in Numerical Mathematics Vol. 140/141 (Birkhauser, Basel, 2001); J. D. Au, M. Torrilhon, and W. Weiss, Phys. Fluids **13**, 2423 (2001).
[42] H. Struchtrup and M. Torrilhon, Phys. Fluids **15**, 2668 (2003); J. Fluid Mech. **513**, 171 (2004).